AIAA JOURNAL
Vol. 43, No. 10, October 2005

Evaluation of Near-Wall Turbulence Models for Deliberately Roughened Liquid Annular Seals

L. A. Villasmil,* H. C. Chen,† and D. W. Childs‡
Texas A&M University, College Station, Texas 77843

An extensive numerical evaluation of the performance of two near-wall treatments and two core-flow turbulence models has been done while simulating experimental tests of water flowing between flat plates with deliberately roughened surfaces. These flat-plate tests replicated the results of several annular seal experiments in which friction factor increased as the seal clearance increased. Annular seals are extensively used in a wide range of turbomachinery, and their design influences efficiency and rotordynamic stability. A commercial code, FLUENT, was used to solve the Reynolds-averaged Navier–Stokes equations with the flat-plate tests as a reference. The performance of the standard wall functions, based on the law of the wall, as near-wall treatment of turbulence was evaluated and compared to the two-layer-zonal approach. Similarly, the solutions obtained with the standard and "renormalization group" method versions of the first-order closure k–ε model were contrasted to those obtained with a second-order closure, the Reynolds-stress model. Although the main features of the friction factor behavior observed in the experiments under study were reproduced with a simple two-dimensional approach, the present work concentrates on the numerical detail and lessons learned while obtaining such results. It was found that wall function solutions are extremely sensitive to the location of the first grid point near the wall, even if it is located within the overlap region. In addition, the low-Reynolds nature of the flow requires coarse meshing making any k–ε model solution grid dependent. On the other hand, the two-layer zonal model is more consistent, and it is not sensitive to the location of the first grid point near the wall, provided it is located at a y^+ distance no larger than 10. Solutions obtained with the latter approach and the Reynolds-stress model are found to be grid independent. In summary, a numerical solution is truly grid independent when it is consistently replicated upon variation of the discretization scheme, the pressure-to-velocity linking method, the algebraic equation solving algorithm, and the mesh size and type. In low-Reynolds-number turbulent flow, the two-layer zonal approach fulfills such statement as near-wall treatment of turbulence.

Nomenclature

a	=	flat-plate tester clearance
f	=	Darcy friction factor based on twice the clearance as the hydraulic diameter
k	=	turbulent kinetic energy
L_x	=	streamwise length
$\dot{m}_L$	=	mass flow rate per unit width, kg/(s · m)
R, $\bar{R}$	=	convergence residual, normalized residual
Re, Re_N	=	Reynolds number, numerical Re (simulation mass flow rate given an experimental pressure gradient)
r	=	ratio of geometric expansion
T	=	water temperature
U^*	=	$U_p \cdot C_\mu^{1/4} \cdot k_p^{1/2}/(\tau_w/\rho)$
y^+, y^*	=	wall unit distance, $\rho \cdot C_\mu^{1/4} \cdot k_p^{1/2} \cdot y_p/\mu$
ΔP_x	=	streamwise pressure gradient
Δw	=	grid (cell) dimension in the direction normal to the wall
Δx	=	grid (cell) dimension in the x direction
Δy	=	grid (cell) dimension in the y direction
ε	=	turbulence dissipation
μ	=	water viscosity
ρ	=	water density

Presented as Paper 2003-3741 at the AIAA 33rd Fluid Dynamics Conference, Orlando, FL, 23–26 June 2003; received 8 December 2003; revision received 9 February 2005; accepted for publication 27 February 2005.

*Graduate Assistant Research, Turbomachinery Laboratory. Student Member AIAA.
†Professor, Department of Civil Engineering. Senior Member AIAA.
‡Professor, Department of Mechanical Engineering.

Introduction

In general, rotor surfaces of annular seals in most turbomachinery are smooth. On the other hand, these smooth rotors have been combined with labyrinths and different roughness pattern stators to reduce leakage and enhance rotor response. In 1982, Von Pragenau[1] proposed a roughened-stator seal to improve the vibration characteristics of the liquid fuel-rocket engine turbopumps. Experimentalists traditionally evaluate and compare leakage performance of different seal arrangements by generating friction factor curves vs Reynolds number. Recent static tests of honeycomb annular gas seals by Al-Qutub et al.[2] confirmed what previous experiments by Ha and Childs[3] in 1992, DeOtte et al.[4] in 1994, and Childs and Fayolle[5] in 1999 found, that friction factor increases with clearance. Although some researchers have successfully reproduced some of these experiments with numerical techniques like the original work of Chochua et al.,[6] none of them has addressed the issue of the friction-factor-to-clearance proportionality behavior.

Present numerical computations were based on the experimental work of Nava[7] and Hess,[8] who performed flat-plate experiments, finding that friction factor increased as the clearance increased, reached a maximum at a certain intermediate clearance, called the "plateau," and decreased as the clearance was increased further. Figure 1 shows numerical periodic units and dimensions of the two largest roughness patterns tested in the experiments. (The smooth top walls are removed.) Their work included additional tests performed with roughness patterns half the size of these geometries. For complete details of their test apparatus, experimental data, and entry data for numerical simulations, see Refs. 7–9.

Regarding numerical computations and modeling of turbulence, most researchers rely on the standard k–ε model with the wall function approach.[10] Numerically, this approach is very stable. However, from a physical point of view it cannot adequately calculate flows with significant mean streamline curvature, separation, low Reynolds number, and recirculation.[11] All of these flow characteristics are present in annular seals with deliberately roughened

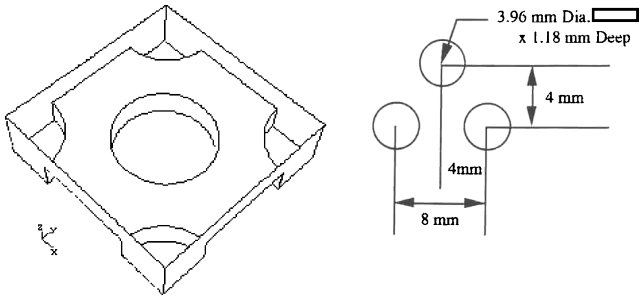

a) Large round-hole geometry

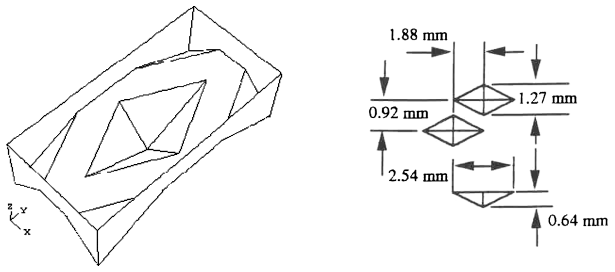

b) Large knurl geometry

Fig. 1 Nava[7] and Hess[8] large roughness patterns.

surfaces, making the accuracy of the near-wall treatment of turbulence a critical factor. Several attempts have been made to develop models that are valid all of the way to the wall. Patel et al.[12] evaluated the performance of many low-Reynolds number and near-wall extension turbulence models and concluded that none was completely successful in predicting the features of the flow close to a solid wall. In 1987, Patel and Chen[13] introduced a two-layer formulation to resolve the turbulent wake of a flat plate that was further improved in Chen and Patel,[14] combining the standard k–ε model with the one-equation model of Wolfshtein.[15] They concluded that the two-layer model outperformed any low-Reynolds-number model.

Numerical Approach

Nava[7] and Hess[8] performed approximately 40 runs per each plate combination, small round-holes against smooth walls, large round-holes against smooth walls, small knurls against smooth walls and large knurls against smooth walls; for six clearances, ranging from 76 μm (3 mils) to 1270 μm (50 mils), and Reynolds number of 1.51×10^3 to 6.05×10^4 (Table 1).

Because of the heavy computational effort initially estimated to replicate all experiments, the numerical approach was planned as follows: 1) steady two-dimensional simulations with the laminar-flow model; 2) steady two-dimensional simulations with turbulent-flow models; 3) unsteady two-dimensional turbulent-flow model simulations; and 4) three-dimensional simulations, steady and unsteady as dictated and led by the two-dimensional results.

More than 1500 simulations were performed solely in the two-dimensional approach covering the experimental flow range and beyond, all six clearances and the two roughness patterns, including two additional sizes per roughness. Three-dimensional simulations were halted on time constraints and the success of the two-dimensional approach in qualitatively reproducing the plateau effect and the friction factor to clearance proportionality.

In terms of the computational domain, a periodic unit approach was used. Roughness patterns on a plate's surface promote fluid mixing, and under the steady flow regime the fully developed flow condition is achieved after the flow has entered the plate gap and passed through few roughness patterns. In the original experiments, most pressure drop curves are linear within pressure taps, indicating a constant pressure gradient in the streamwise direction, a characteristic of fully developed periodic flow. Patankar et al.[16] originally proposed the periodic developed flow formulation for incompressible flow in 1977. The periodic approach implies that velocity components and turbulent quantities repeat themselves but not the pressure.

Table 1 Nava[7] and Hess[8] experimental data range

Clearance, μm (mil)	Re	f	Pressure gradient, kPa/m
	Small round hole		
76 (3.0)	5,503–12,959	0.0052–0.0047	9,098.9–44,475.7
127 (5.0)	7,568–16,008	0.0141–0.0134	8,373.5–33,157.3
254 (10.0)	1,884–13,152	0.0323–0.0098	434.9–7,159.6
508 (20.0)	1,929–23,734	0.0642–0.0218	94.1–5,104.3
762 (30.0)	1,923–29,262	0.1539–0.0337	50.1–3,247.6
1270 (50.0)	2,235–60,531	0.1914–0.0297	16.8–2,670.5
	Large round hole		
76 (3.0)	8,355–15,252	0.0023–0.0020	8,159.5–24,213.6
127 (5.0)	10,632–15,961	0.0048–0.0046	6,146.3–13,028.6
254 (10.0)	2,318–13,027	0.0409–0.0179	613.4–7,747.3
508 (20.0)	1,594–20,444	0.0682–0.0250	104.9–6,077.1
762 (30.0)	2,297–37,061	0.0698–0.0351	49.9–4,802.1
1270 (50.0)	1,904–57,917	0.0941–0.0299	9.8–3,508.7
	Small knurl		
76 (3.0)	3,043–8,653	0.0316–0.0156	12,668.2–52,735.1
127 (5.0)	5,956–9,611	0.0360–0.0230	12,663.0–26,994.5
254 (10.0)	1,598–5,958	0.0779–0.0367	966.3–8,880.7
508 (20.0)	1,510–15,188	0.0926–0.0476	151.7–6,730.3
762 (30.0)	1,675–25,353	0.0835–0.0424	44.2–4,749.5
1270 (50.0)	1,649–50,606	0.1967–0.0370	14.0–2,588.6
	Large knurl		
76 (3.0)	2,462–6,915	0.0446–0.0159	17,496.8–57,917.8
127 (5.0)	8,279–11,842	0.0382–0.0285	14,182.6–30,638.9
254 (10.0)	2,705–15,307	0.1146–0.0311	1,087.2–9,032.4
508 (20.0)	1,968–19,678	0.1106–0.0592	174.5–7,739.8
762 (30.0)	2,090–33,438	0.1123–0.0524	50.8–5,462.0
1270 (50.0)	2,203–57,278	0.1373–0.0461	NA–2,977.0

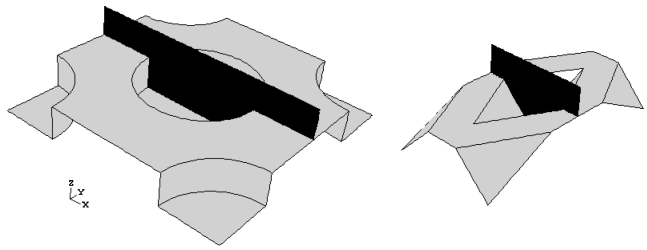

Fig. 2 Two-dimensional periodic units; small round hole and large knurl. Clearance ($a = 508$ μm).

Instead, the pressure drop is periodic and implemented as follows:

$$\nabla P(\boldsymbol{r}) = \beta \cdot \boldsymbol{L}/|\boldsymbol{L}| + \nabla \tilde{P}(\boldsymbol{r}) \tag{1}$$

Term β represents the linear varying pressure gradient along the periodic unit domain, which is prescribed, and L the physical length in the streamwise direction of the computational domain. The second term in Eq. (1) represents the truly periodic pressure gradient. Figure 2 shows as darkened surfaces the two-dimensional periodic units of the small round-hole and the large knurl patterns, which indeed are symmetry planes of each three-dimensional roughness computational domain, where the spanwise mean flow and mean gradients are assumed to be negligible. The relative size of the geometries and the clearance between the plates are shown to scale, but the top smooth walls that contain the pressure taps were removed.

Grid-Independent Solutions and Convergence

The numerical approach followed in this research was oriented to obtain solutions that reflect the flow physics observed in the experimental data and were independent of the grid size and type. Starting from coarser grids and simple discretization schemes, the size of the grid was reduced, and higher-order discretization schemes were implemented to generate laminar solutions when the experiments reflected such behavior and to have consistent predictions in the turbulent cases. Flow in an annular seal is normally turbulent; therefore, most of the research analysis concentrated in the turbulent flow cases. Figure 3 shows the basic grid meshing types used.

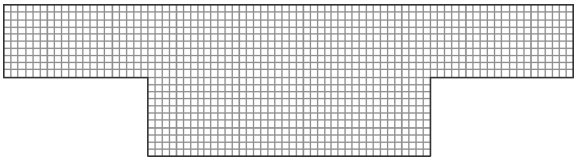

a) Uniform, $\Delta x = \Delta y \approx 50\ \mu$m (MU 50)

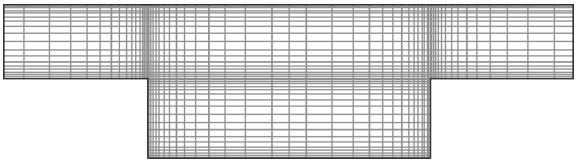

b) Boundary layer, $\Delta w = 10\ \mu$m, $r = 1.25$ (BL 10 1.25)

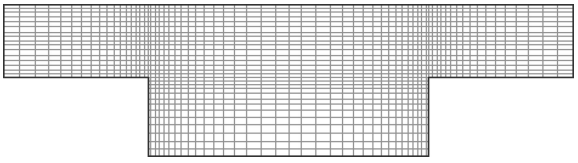

c) Boundary layer, $\Delta w = 25\ \mu$m, $r = 1.25$ (BL 25 1.25)

Fig. 3 Small round-hole geometry grids ($a = 508\ \mu$m).

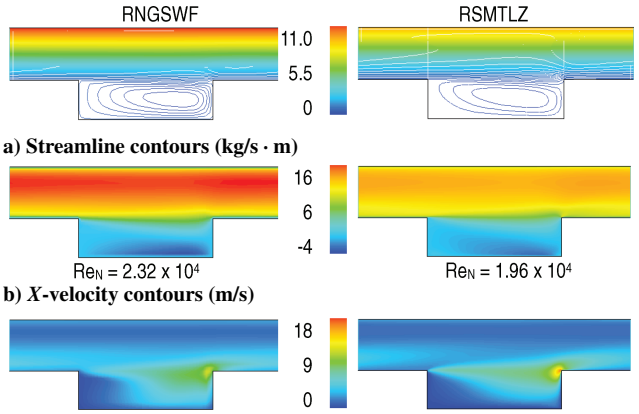

a) Streamline contours (kg/s · m)

b) *X*-velocity contours (m/s)

c) Turbulent kinetic energy contours (m^2/s^2)

Fig. 4 Mean flow features, small round-hole geometry.

Initial grid-independent solution studies concentrated in mass flow rate convergence and the stabilization of some turbulent quantities. Numerical grid of pilot cases started with coarse and uniform spacing but ended with fine spacing clustered to the wall in a boundary-layer style, to reduce the total number of nodes while concentrating them in the regions characterized by high gradients. The grid-refinement study demanded physical spacing so small that the geometric tolerance of the grid-generation software was reached (GAMBIT version 1.3.0). This geometric tolerance was equivalent to 2 μm. Thus, most numerical cases were run with grids where the first point closest to the wall was located at this geometric tolerance.

Figure 4 compares the mean flow features predicted in the small round hole using the renormalization group (RNG) k–ε model and the standard wall function (SWF) approach (RNGSWF), against the results obtained with the Reynolds-stress turbulence model (RSM) and the two-layer zonal (TLZ) approach (RSMTLZ), while fulfilling the wall distance criteria of the first grid point location. Both solutions are qualitatively comparable, although the RNGSWF model predicts a stronger recirculation within the hole, whereas the RSMTLZ model predicts secondary recirculation zones, not shown, at the leading edge and the bottom corners of the round hole. The mean flow separates at the leading edge of the round hole and does not enter in it, although the interface with the recirculation zone slightly moves inward, because of the enhanced turbulence activity that initiates at the leading edge and increases monotonically while the mean flow moves toward the trailing edge.

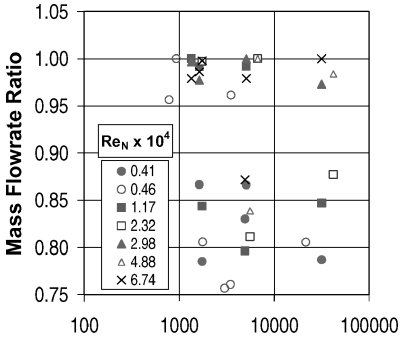

a) Grid size (nodes)

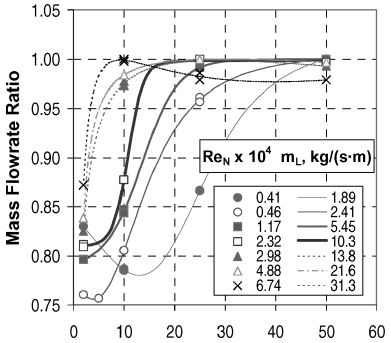

b) Grid size, μm

Fig. 5 Small round-hole grid-independent solution analysis, RNGSWF approach.

Figure 5a shows how the nondimensional mass flow rate (actual flow rate divided by the maximum among all grid solutions for each case) of the small round-hole geometry changes with grid refinement in terms of number of nodes for several numerical Reynolds number and clearance cases ran with the RNGSWF model combination. No clear trend is observed. However, when the same data are outlined considering the distance to the wall of the first grid point, a clear pattern emerges.

Figure 5b explains why the geometric tolerance was reached while looking for grid-independent solutions. Continuous lines indicate grid solution trends of cases based on experimental data, whereas dotted lines are results obtained for Reynolds number beyond the experimental range (increasing the pressure gradient across the periodic boundaries). At low Reynolds numbers (cases below 2.32×10^4), coarse grid solutions (a 50-μm uniform spacing allows only 10 nodes across the clearance of 508 μm as shown in Fig. 3a) appear to require further refining, as the computed mass flow rate either stabilizes at lower grid sizes or reduces continuously without stabilization. Test cases with larger Reynolds numbers outside the experimental range (2.98×10^4 and above) were run, and they indicated that solutions with the 50-μm grid ($y^+ \sim 20$–100) could be considered grid independent in terms of mass flow rate for Reynolds numbers larger than 2×10^4–3×10^4.

In summary, maximum flow rates for the round-hole geometries were consistently found, given a pressure gradient value, in grid solutions where y^+ varied from 10 to 40 when the RNGSWF turbulence approach was used. On the other hand, maximum flow rates of the knurl geometries were normally found in the coarsest grids with y^+ ranging from 40 to 80.

In contrast to RNGSWF results, Fig. 6 shows how the nondimensional mass flow rate of the same geometry is relatively stable and consistent as the grid is refined when using the RSMTLZ turbulence model combination. Comparable mass flow rates were obtained even in cases where the first grid point near the wall was outside the viscous sublayer ($y^+ \sim 5$), which was the normal case in grid sizes of 25 μm and larger for all Reynolds numbers. Observed deviations hardly exceeded 5%. Given a pressure gradient value, maximum flow rate was normally found in grid solutions where the first point was located well inside the viscous sublayer ($0.5 < y^+ < 1.0$). Although in few cases, maximum flow rate was

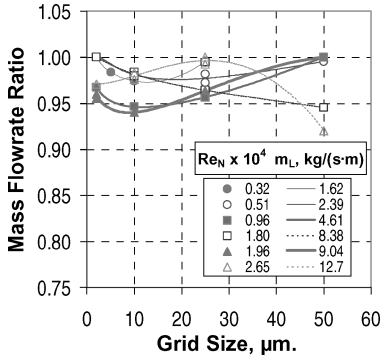

Fig. 6 Small round-hole grid-independent solution analysis, RSMTLZ approach.

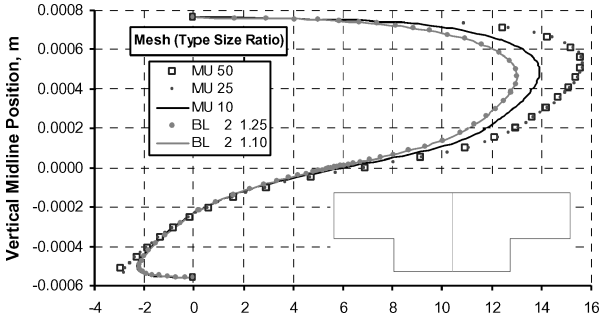

a) Velocity, m/s

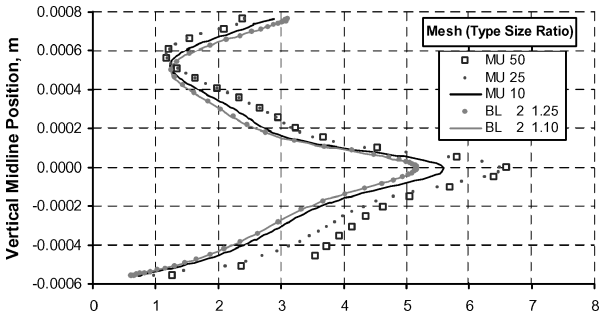

b) Turbulent kinetic energy, m^2/s^2

Fig. 7 RNGSWF model profiles; $Re_N = 2.32 \times 10^4$. Small round-hole geometry; $a = 762$ μm.

found in grids with the first grid point located well outside such layer ($14 < y^+ < 22$).

In addition, profiles of several flow properties were examined among the several grids used to ensure that a grid-independent solution was obtained.

Figure 7a shows vertical midline x-velocity profiles of all grid cases corresponding to a Reynolds number equal to 2.32×10^4 in Fig. 5b. MU50 ($y^+ \sim 20$–25) and MU25 ($y^+ \sim 9$–13) solutions are comparable (within 1% in most of the domain), an indication of grid-independent results. It should be noted how the profile differs for the rest of the solutions: BL2 ($y^+ \sim 1.0$) are identical, whereas MU10 ($y^+ \sim 4$–5) stands alone. In contrast, turbulent kinetic energy profiles in Fig. 7b indicate that MU50 and MU25 solutions are comparable within the plate clearance, whereas they differ slightly (2%) at the clearance-hole interface, but noticeable within the hole (up to 31%). Therefore, MU50 and MU25 solutions are still grid dependent.

Figure 8 shows the results obtained with RSMTLZ model for the same pressure gradient and geometry conditions of results shown in Fig. 7 (Re_N equal to 1.96×10^4 in Fig. 6). In this case, all solutions are comparable, but the coarsest grid MU50 ($y^+ \sim 18$–22) x-velocity profile differs slightly from the rest, mainly within the clearance (up to 3%). Similarly, turbulent kinetic energy profiles in Fig. 8b indicate that all solutions except MU50 are comparable. MU50 solution does not show a peak near the top wall, and deviations are up to 15%.

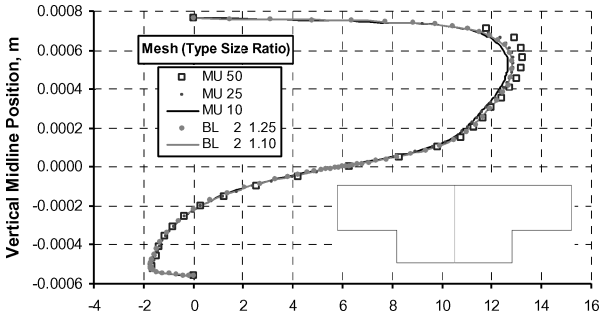

a) Velocity, m/s

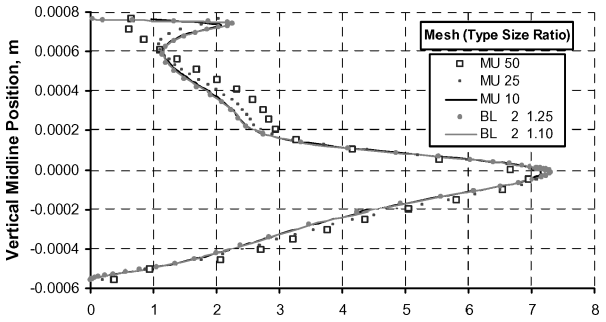

b) Turbulent kinetic energy m^2/s^2

Fig. 8 RSMTLZ model profiles; $Re_N = 1.96 \times 10^4$. Small round-hole geometry; $a = 762$ μm.

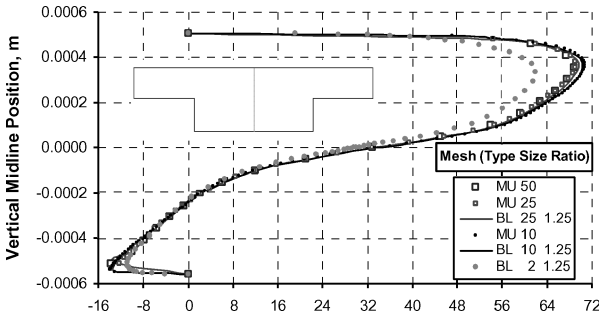

a) Velocity, m/s

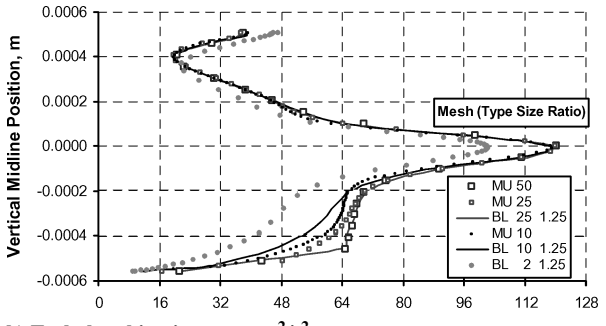

b) Turbulent kinetic energy m^2/s^2

Fig. 9 RNGSWF model profiles; $Re_N = 6.74 \times 10^4$. Small round-hole geometry; $a = 508$ μm.

Although comparable, MU25 ($y^+ \sim 10$–12) solution clearly differs within the clearance and the hole (up to 8%). MU10 ($y^+ \sim 4$–5) and both BL2 ($y^+ \sim 0.8$–1.0) solutions are nearly identical, an indication that MU10 is grid independent.

The general trends of the cases just discussed were observed repeatedly among all simulations performed in all geometries. Although results with the more elaborated RSMTLZ model were consistent and grid independent for a range in wall units of roughly 1.0 to 10, solutions obtained with the RNGSWF model are inconsistent and often grid dependent.

Figure 9a shows vertical midline x-velocity profiles of all grid cases of the artificial high Reynolds number of 6.74×10^4 in Fig. 5b.

All solutions except BL2 ($y^+\sim4.0$) are comparable within 2%, an indication of grid-independent results. Similarly, in Fig. 9b turbulent kinetic energy profiles of all solutions are within 3% in most of the domain, but only MU50 ($y^+\sim76$–96) and BL25 ($y^+\sim38$–46) solutions are identical in the whole domain (within 1%). Note that MU25 ($y^+\sim38$–46), and BL25 solutions differ up to 10% within the hole. Recalling Fig. 3c, the first nodes near the bottom wall in the BL25 grid are located at approximately 54 μm (and not 25 μm), just as the ones of the MU50 grid are effectively located at 51 μm. MU50 and BL25 could be considered grid-independent solutions, but their similarities are associated by matching the location of the first grid points near the bottom wall of the hole.

All RNGSWF solutions appear to be grid dependent when the first grid point near the wall is located at a wall unit distance of 50 or less, and the numerical results are particularly influenced by the location of this first grid point.

Regarding numerical convergence in terms of residual errors, the mass flow rate residual was consistently the driver of the convergence process in the iterative solution of all simulations performed. Software default options of scaled residuals were maintained for all variables. The software scaling procedure for the mass flow rate or continuity residual is not typical, and the actual formula is

$$\bar{R} = \frac{R(N)}{R(5)} \tag{2}$$

$$R(I) = \sum_{\text{cells}} |\Delta \dot{m}(I)| \tag{3}$$

The numerator represents the total mass imbalance in the domain at iteration N, and the denominator is the largest absolute value of the continuity residual in the first five iterations. The default convergence criterion in the software is 0.001 for all scaled residuals. Literature recommends monitoring variables in an integral way rather than single-point monitoring. Figure 10 shows the convergence study performed in the 254-μm (10-mil) clearance of the small round-hole geometry. On the figure, the pressure gradient represents the ratio between the numerically integrated pressure gradient (shear and pressure forces in the streamwise direction) and the experimental pressure gradient. In addition, the mass flow rate is the ratio between the actual mass flow rate and its value at the last residual level in the plot.

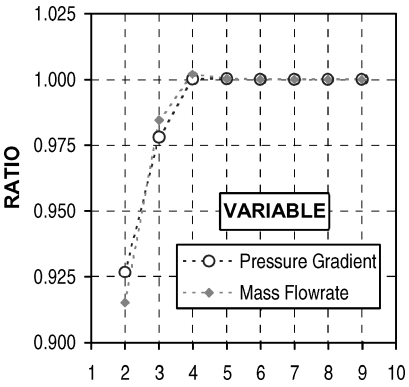

a) Residual [-LOG(R)]

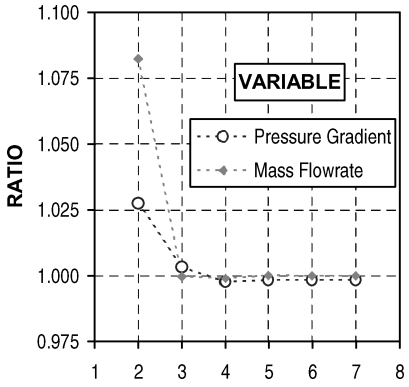

b) Residual [-LOG(R)]

Fig. 10 Residual convergence history: a) RNGSWF model and b) RSMTLZ model.

Clearly, a minimum residual of 10^{-5} is required to achieve convergence when the RNGSWF turbulence model is used. Nearly all simulations performed with this model exhibit this behavior. When the turbulence model is switched to the RSMTLZ, the solution ceases to vary at a continuity residual of 10^{-4}, one order of magnitude larger.

Turbulence Modeling Comparison

Figure 11 combines grid solutions of Figs. 7a and 8a to contrast the results obtained with both turbulence models. MU50 solution complies with the modeling restriction of the law of the wall approach, and it is 22% larger than any BL2 solution obtained with the two-layer zonal approach. Nonetheless, all BL2 solutions are comparable within 4% in spite of the difference in turbulence modeling, and that the location of the first grid point violates the law of the wall requirements in the RNGSWF model. BL2 grids have several points located in the viscosity affected region, and the software adjusts the velocity profile near the wall depending on the location of the first grid point ($U^* = y^*$ for $y^* < 11.225$), when using the SWF approach.

Finding that k–ε model predictions in terms of mass flow rate for this geometry, with the law of the wall mistakenly applied well inside the overlap region, are comparable with those obtained with the more elaborated Reynolds-stress model with the two-layer zonal approach was surprising. Several additional cases were run to clarify the effect of the turbulence models and each near-wall treatment in the friction factor predictions. The same experimental cases were run in three modeling combinations with identical grid BL2 and discretization schemes, second-order upwind for all variables and simple C pressure-velocity linking algorithm (SOUC): first, the RNG k–ε for turbulence modeling and SWF for the near-wall treatment. Second, while retaining the RNG k–ε for the core region, the SWF approach was replaced by the TLZ model. Finally, the RNG k–ε was switched to the RSM model for the core region employing the TLZ model at the wall.

Figure 12 compares vertical midline profiles between turbulence models and near-wall treatment in the final grid (BL2, $y^+\sim0.8$–2.0) of the small knurl geometry case for an intermediate clearance of 762 μm (30 mil) and the pressure gradient corresponding to the largest experimental Reynolds number. An additional coarse grid solution is included (MU50, $y^+\sim18$–22) as a reference.

The x-velocity profiles of the BL2 RNGSWF and RSMTLZ solutions in Fig. 12a are not as close as in the small round-hole geometry. In the small knurl geometry, they differ up to 7%. On the other hand, the effect of locating the first grid point too close to the wall is to scale down the x velocity in 16% (MU50 vs BL2, RNGSWF model). Similarly, the BL2 RSMTLZ solution x-velocity profile is 15% lower than the BL2 RNGTLZ solution.

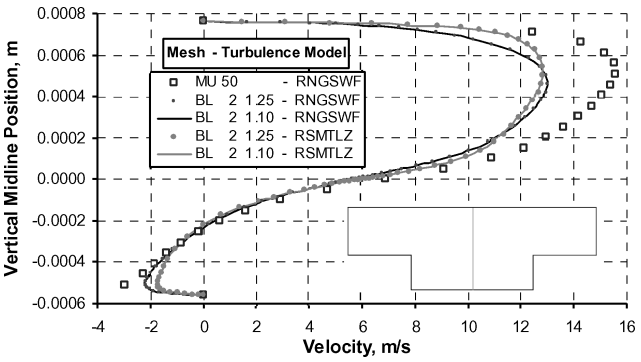

Fig. 11 X-velocity profiles, small round-hole geometry; $a = 762$ μm; RNGSWF $Re_N = 18.88 \times 10^4$; RSMTLZ $Re_N = 1.96 \times 10^4$.

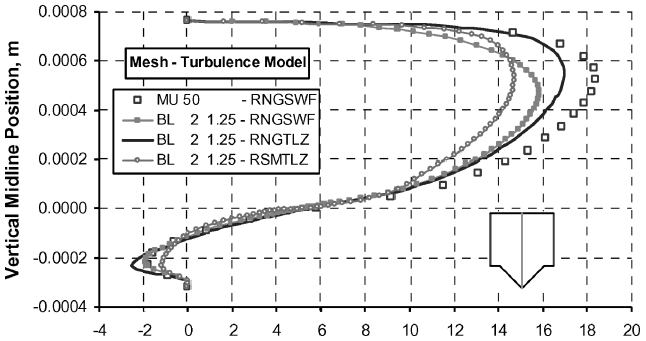

a) Velocity, m/s

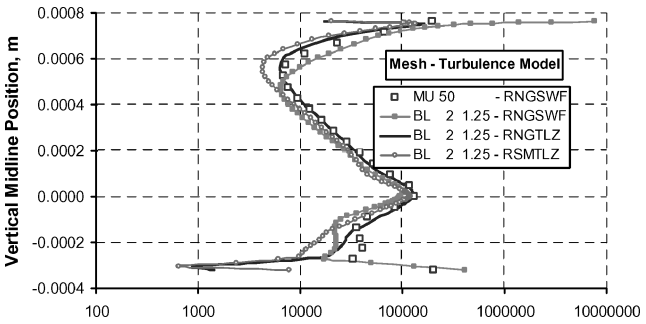

b) Dissipation, m^2/s^3

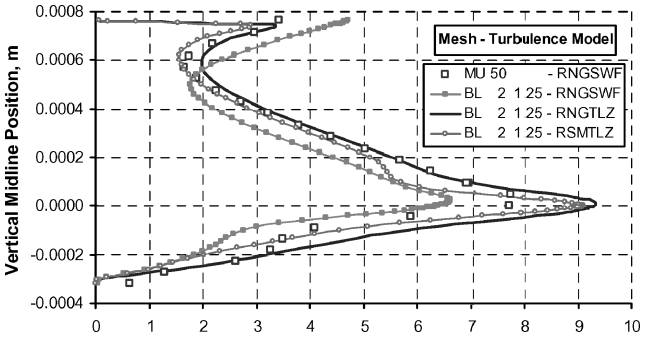

c) Turbulent kinetic energy, m^2/s^2

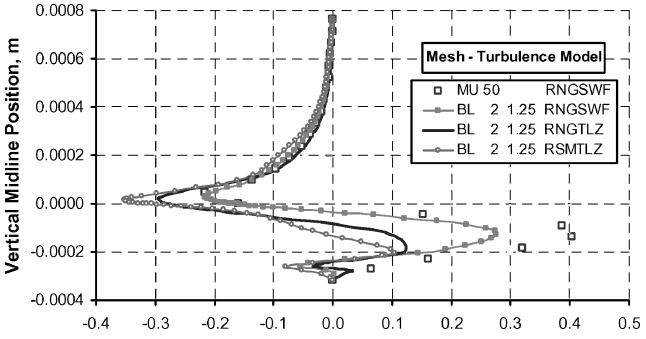

d) Vertical velocity, m/s

Fig. 12 Turbulence modeling comparison; $Re = 2.53 \times 10^4$. Small knurl geometry; $a = 762$ μm.

Figure 12b shows turbulent dissipation profiles. They are comparable near the clearance-hole interface (zero y coordinate) but differ greatly near the top wall and inside the knurl. At this interface, RNGTLZ and RSMTLZ are within 3%, and both exceed the BL2 RNGSWF by more than 20%, but MU50 is only 9% larger. Near the top wall, RNGTLZ predictions exceed those of the RSMTLZ within 20–40%, RNGTLZ and MU50 are comparable, but the BL2 RNGSWF values are at least one order of magnitude larger. At the bottom corner, a similar behavior is observed; both RNGWF solution values are two orders of magnitude larger than any TLZ solution values.

In Fig. 12c, turbulent kinetic energy levels in the whole region are comparable within an average 20% with the exception of the BL2 RNGSWF solution, which is up to 40% near the top wall and down 30% at the interface. Noteworthy is the hybrid effect observed in the RNGTLZ solution. While near the walls, RNGTLZ predictions resemble the RSMTLZ shape profile; those predictions are like the RNGSWF profile in the core region.

Vertical velocity profiles shown in Fig. 12d are comparable within the clearance, but all predictions differ from each other up to 40% in average at the interface and within the knurl.

It is apparent that a compensating effect makes k–ε and Reynolds-stress models predictions comparable for grids with $y^+ \sim 1.0$. In the former type, turbulence is underpredicted in the core region, but such underprediction is adjusted when the location of the first grid point well inside the overlap region numerically enhances the turbulent activity near the wall. The net effect is to observe comparable mass flow rates and friction factors.

Upon scrutiny of the software treatment of the boundary conditions for the dissipation equation, it was found that the dissipation value at the first grid point is explicitly calculated, and it is inversely proportional to the distance to the wall. Unlike the friction velocity adjustment, no compensation is included in the dissipation value at the boundaries when the first grid point is located inside the viscous sublayer.

Figure 13 compares the mean flow features predicted in the small knurl using the RNGSWF model with the results of the RNGTLZ combination, against those obtained with the RSMTLZ approach, for the same case described in Fig. 12 (a given pressure gradient of 4749.5 kPa/m). Both RNG solutions are comparable, although the RNGTLZ combination predicts slightly larger turbulent kinetic energy levels. The RSMTLZ approach predicts a weaker recirculation zone but with stronger curvature and the largest turbulent kinetic energy levels overall. In all cases, the mean flow separates at the leading edge of the knurl and does not enter in it, but the interface with the recirculation zone slightly moves inward, an effect clearly observed in both TLZ predictions. The fact that the numerical Reynolds number for the RSMTLZ model is the lowest is an indication that this approach predicts the largest friction factor of all combinations tested.

Additional numerical tests were performed to evaluate if the discretization formulation could influence the results depending on the turbulence model and the grid size. Figure 14a compare x-velocity profiles among three grid solutions, MU50, BL2 1.10, and 1.25,

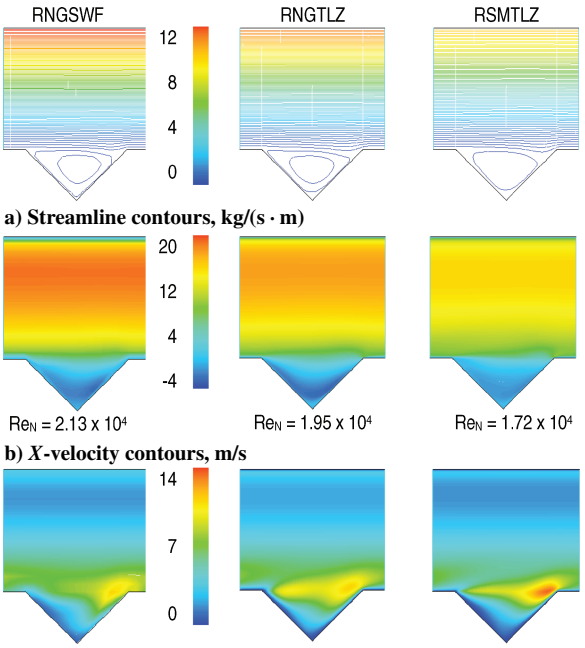

a) Streamline contours, kg/(s · m)

b) X-velocity contours, m/s

c) Turbulent kinetic energy contours, m^2/s^2

Fig. 13 Mean flow features, small knurl geometry.

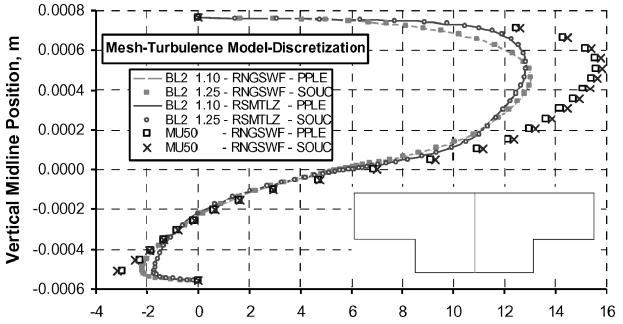

a) Velocity, m/s

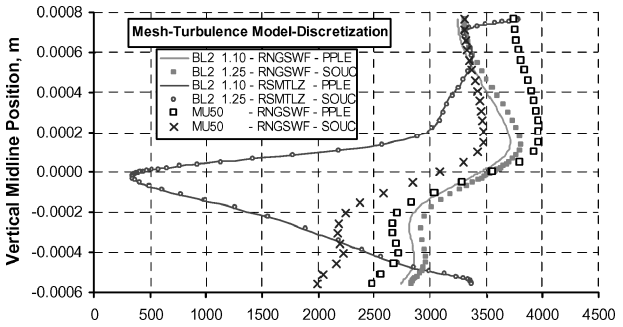

b) Periodic static pressure, Pa

Fig. 14 Discretization scheme effect in the solutions. Small round hole; $Re = 2.93 \times 10^4$; $a = 762$ μm. PPLE, Presto scheme for pressure, power law for velocities, and simple pressure-velocity linking algorithm.

using two discretization schemes. Both BL2 solutions ($y^+ \sim 1.0$) are nearly identical within turbulence models. MU50 solutions ($y^+ \sim 20$–25) are comparable within 2% in the clearance and within 8% in the hole. Figure 14b compare periodic static-pressure profiles among the same grids. Both BL2 solutions for the RSMTLZ model are nearly identical. Likewise, both BL2 solutions for the RNGSWF are comparable within 4%. MU50 solutions differ by 14% in the clearance and by as much as 22% in the hole. RSMTLZ model results are numerically consistent and independent of the discretization scheme and grid expansion ratio. RNGSWF model solutions are sensitive to the grid size and discretization schemes, particularly when a coarse grid is required to comply with the log-law distance to the wall.

Periodic and Steady-State Approach Validation

The pressure gradient in the original experiments was determined from pressure drop measurements along a pair of 13 equally spaced pressure taps located on the smooth surface of the plate arrangement. Most pressure drops against axial position curves are straight lines indicating that the pressure gradient is constant along the plates. A constant pressure gradient confirms that the plate entrance effect is negligible and the flow can be considered fully developed.

To validate the periodicity approach from a numerical point of view, the periodic unit domain of several cases was duplicated along the streamwise direction. Simulations were performed in the large knurl and large round-hole pattern geometries for all clearances, maintaining the same numerical approach (discretization scheme, relaxation factors, turbulence model, grid size, and type) to allow a direct comparison with the results of the single periodic unit. RNGSWF simulation results in terms of mass flow rate of the doubled periodic unit vs the single one of each large pattern geometry are presented in Fig. 15, for all 1270-μm (50-mil) clearance cases.

All simulations on both doubled geometries determined flow rates within 1% of the results of each single periodic unit counterpart, indicating that the periodic approach is valid and that fully developed periodic flow is really achieved in all cases. Similarly, several profiles of turbulent quantities among characteristic lines of the periodic units were compared and resulted in identical curves. Numerical solutions are repeated from one periodic unit to the next.

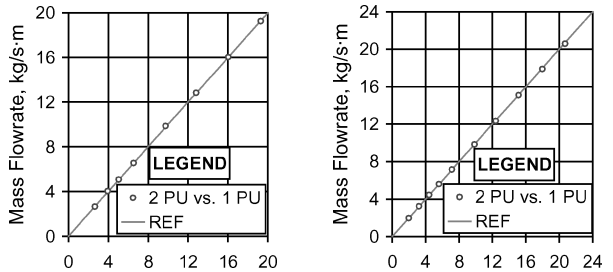

a) Mass flow rate, kg/(s · m) b) Mass flow rate, kg/(s · m)

Fig. 15 Doubled vs single periodic unit mass flow rate; a) large knurl and b) large round hole.

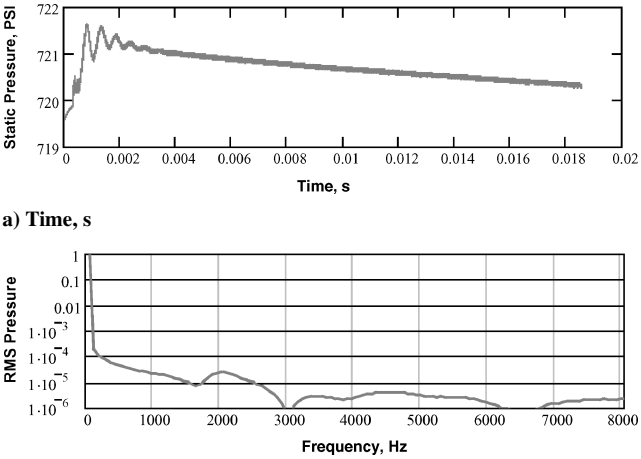

a) Time, s

b) Frequency, Hz

Fig. 16 Unsteady analysis, small round-hole; $a = 762$ μm: a) tap static pressure and b) normalized fast Fourier transform.

Regarding the steady-state approach, the possibility of unsteady flow within the plates was observed by Hess[8] in the original experiments. He indicated in the dynamic pressure analysis on the experimental data of Nava[7] that the spectra for the shallow cavities, small round hole, showed evidence of lateral resonance characterized by multiple modes of oscillation believed to be driven by flow instabilities. An unsteady analysis was performed in the two-dimensional small round hole for clearance and closest Reynolds number described in his work. First- and second-order temporal discretization were used with a time step small enough to capture the frequency ranges observed in the experiments. The numerical static pressure was obtained in a point approximately located at the pressure tap location on the top wall.

Figure 16 shows the unsteady analysis results obtained with the RSMTLZ modeling approach. The numerical procedure reduces to activate the temporal solution algorithm starting from a steady-state converged solution. The few oscillations observed correspond to the numerical perturbation introduced when switching solution algorithms. Once the perturbation disappears, the unsteady algorithm converges to the initial steady-state solution. An indication that oscillations observed experimentally are either not reproduced by the model or are not associated with fluid instabilities in the flow itself, but with the resonance effect within the pressure tap hole, an effect that was not totally discarded in the original dynamic analysis.

Comparison to Experiments

All results in the original experiments were expressed in terms of the friction factor and Reynolds number. The present numerical results were expressed in such format with the use of the following formulas derived for channel flow and following the approach of Ref. 7:

$$f = \left[(4 \cdot a^3) \cdot (\Delta P_x / L_x) \cdot \rho(T)\right] \cdot \left(1 \Big/ \dot{m}_l^2\right) \tag{4}$$

$$Re = 2/[\mu(T)] \cdot \dot{m}_l \tag{5}$$

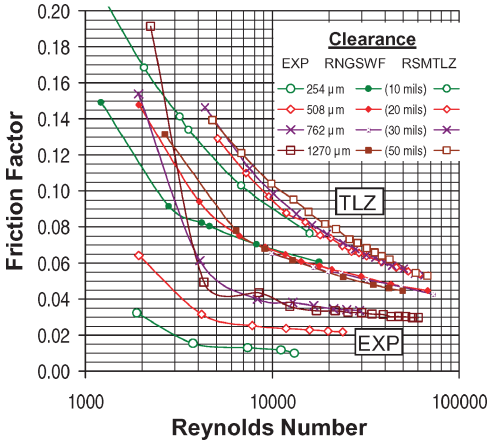

Fig. 17 Friction factor, experiments vs simulations. Small round-hole pattern.

where the expressions between brackets are extracted from the experimental data with a devised reverse procedure to estimate the actual water temperature in the experiments, and $\dot{m}_l$ is the mass flow rate per unit width determined with the computational fluid dynamics software.

Figure 17 compares the experiments for the four largest clearances (turbulent flow) and the numerical results obtained with two model combinations, RNGSWF and RSMTLZ, in the small round-hole geometry, while fulfilling y^+ criteria. Both model simulations clearly overpredict the experimental friction factor, RNGSWF modeling by 60% and RSMTLZ modeling as much as 200%, in the Reynolds-number range of interest, 8×10^3–4×10^4. Certainly, these results could be considered discouraging, but rather than replicate experimental values with a simple two-dimensional approach the primary interest of the present research was to evaluate the ability of several turbulence models in reproducing the friction factor to clearance behavior. Experiments showed a weak Reynolds-number dependence and that friction factor increased with clearance but ceased to increase at the largest clearance. RNGSWF results show comparable Reynolds dependence but no apparent clearance effect. RSMTLZ results indicate a stronger Reynolds-number dependence but reproduce the fact that friction factor increases with clearance, although in a smaller proportion.

All numerical tests performed while simulating several cases in the rest of the geometries confirmed the observed trends in the friction factor. Although RNGSWF solutions, fulfilling the y^+ criterion, appear to neglect the effect from the clearance, RSMTLZ solutions fairly reproduced the proportionality behavior to the actual clearance with best correlation in the knurl geometries, where friction factors were less overpredicted (60–100%). Similarly, RSMTLZ simulations indicated that the maximum friction-factor values corresponded to the large knurl geometry just like the experiments. RSMTLZ results also reproduced the plateau phenomena at the same intermediate clearance of 508 μm (20 mils) in the small knurl geometry and barely in the large one. To provide more insight in the trends observed, more sizes of each pattern were evaluated. The numerical results indicated that for every roughness pattern there is a particular size where the friction factor is the maximum, and it barely varies with changes in clearance. When a larger pattern size is used, the friction factor decreases and becomes directly proportional to the clearance. If a smaller pattern size is used, the friction factor becomes inversely proportional to the clearance, but it has less dependence on the clearance. A complete discussion on the friction factor behavior findings is included in Refs. 9 and 17.

Discussion

All numerical results indicate that k–ε models in combination with standard wall functions predict lower friction factors that any combination using the two-layer zonal approach, while the

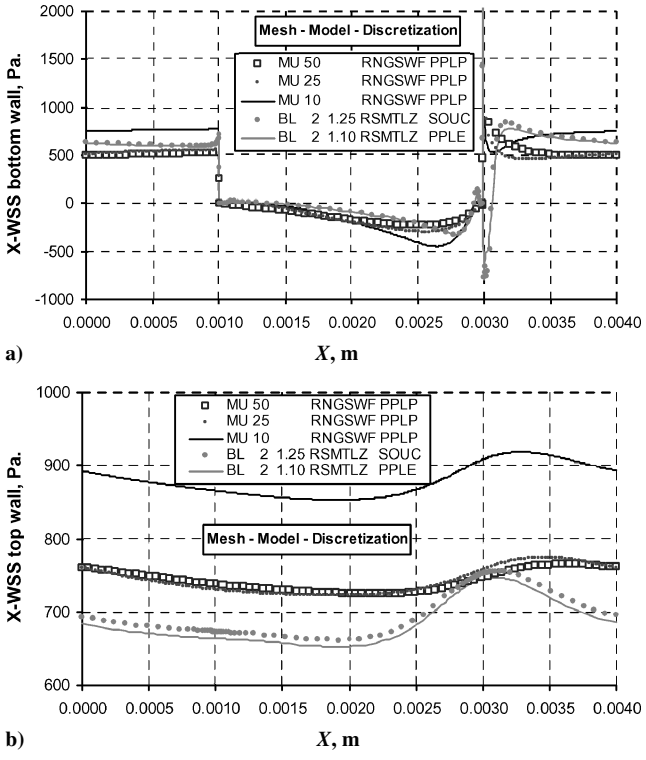

Fig. 18 Streamwise wall shear stress; $Re_N = 2.32 \times 10^4$. Small round-hole geometry; $a = 762$ μm. PPLP, Presto scheme for pressure, power law for velocities, and Piso pressure-velocity linking algorithm.

Reynolds-stress model estimates the largest. In wall-bounded internal flows, the averaged wall shear stress mainly determines the mean pressure gradient. Grid-independent solutions were reviewed to evaluate if the friction factor plateau effect and proportionality behavior observed in the experiments are related to any anomaly in the wall shear stress. No singularities were observed. All profiles collapsed onto a single line indicating self-similarity in the numerical solutions obtained. Scaled profiles reflect the classical cavity flow behavior: a small peak at the leading edge of the either the round hole or the knurl and a high peak located near the trailing edge.[9]

On the other hand, the wall shear-stress profiles analysis among all grid solutions confirmed the compensating effect that makes k–ε model predictions comparable with the more elaborated Reynolds-stress model, when the first grid point is located well inside the viscous sublayer.

Figure 18 present the wall shear stress at the bottom and top walls of the small round-hole geometry for the same case and grid solutions of Fig. 11. Note how MU50 and MU25 profiles are comparable, whereas MU10 clearly overestimates the shear stresses in both walls. RNGSWF (MU50 and 25) and RSMTLZ solutions are comparable, but although RSMTLZ bottom values are smaller, values at the top are larger and show significant peaks on the round-hole edges, even a strong negative peak in the trailing edge. MU10 is the only RNGSWF solution indicating that shear stress reduces after the peak predicted in the trailing edge. The noticeable curvature in the RSMTLZ top values is coupled to these large peaks.

Figure 19 shows enlargements of the stream-function contours plots at the trailing edge of some solutions. As shown in Figs. 19b and 19d, the large negative peaks in the RSMTLZ results are associated with a small but strong recirculation zone generated by the flow separation at the trailing edge after it reattached inside the round hole. No RNGSWF solution could duplicate this negative peak at the trailing edge. The prediction of this strong recirculation zone is related to both: the grid resolution near the wall and the use of the two-layer zonal model.

Similar conclusions are derived from the analysis of the shear-stress profiles in the knurl geometries. Figure 20 shows the bottom

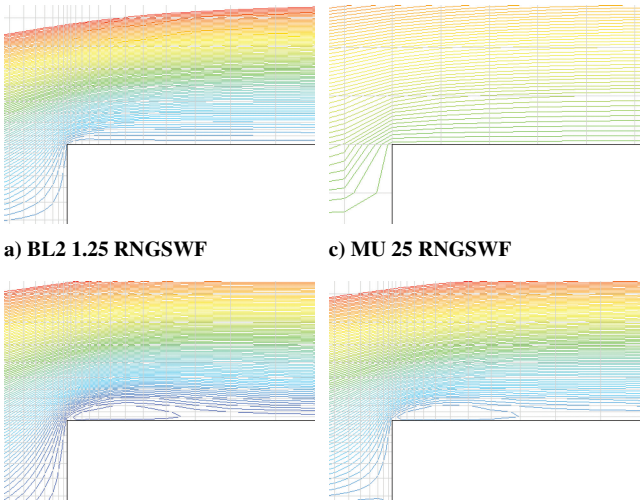

a) BL2 1.25 RNGSWF c) MU 25 RNGSWF

b) BL2 1.25 RSMTLZ d) BL2 1.25 RNGTLZ

Fig. 19 Trailing-edge recirculation detail for several grid solutions, small round-hole geometry.

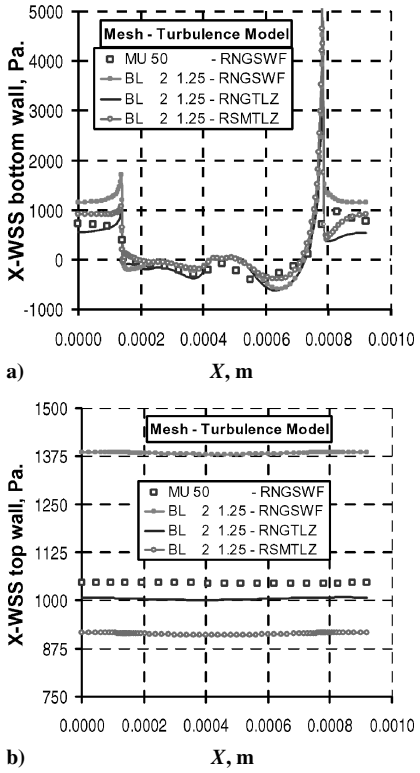

Fig. 20 Streamwise wall shear stress; $Re = 2.54 \times 10^4$. Small knurl geometry; $a = 762$ μm.

and top wall shear stress predicted for the grid solution cases discussed in Figure 12. RNGSWF finest grid solution resembles the RSMTLZ profiles, but actual values are 50% larger.

Conclusions

An extensive analysis has been performed to understand the friction-factor behavior in fluid flow within seals with deliberately roughened surfaces. The results support the following numerical modeling conclusions:

1) The two-dimensional approach overpredicts the friction factor of the experiments for all turbulence models tested.

2) Turbulence models of the k–ε type predict lower turbulence interaction in the core region when compared in similar flow conditions to the Reynolds-stress model.

3) Of the k–ε turbulence models, the so-called renormalization group theory predicts lower friction that the standard model.

4) With all modeling restrictions fulfilled, the Reynolds-stress model predicts higher friction factors than those obtained with any of the k–ε type model.

5) Although the wall function approach as near-wall treatment of turbulence is extremely sensitive to the location of the first grid point near the wall (even if it is located within the overlap region), the two-layer zonal model is consistent, even if the first grid point is located outside the laminar sublayer.

6) Grid-independent solutions could not be consistently found when using the law of the wall and fulfilling its modeling restrictions because of its extreme sensitivity to the location of the first grid and the coarseness required in the grid given the low-Reynolds-number nature of the flow.

7) The consistency of the two-layer zonal approach translates into obtaining well-defined grid-independent solutions. Such consistency is maintained up to $y^+ \sim 10$.

8) The RSMTLZ modeling combination outperformed the RNGSWF approach in reproducing the friction-factor plateau phenomena.

9) A numerical solution is truly grid independent when it is consistently replicated upon variation of the discretization scheme, the pressure-to-velocity linking method, the algebraic equation solving algorithm, and the mesh size and type.

From a physical standpoint, although friction factors obtained with the two-dimensional numerical approach overpredicted the original experimental data, the friction-factor plateau phenomenon and the shift in proportionality of the friction-factor-to-clearance behavior were reproduced, as well as most relative trends. A three-dimensional analysis should lead to better predictions for the friction factor, but there will be a compromise in computer execution time, if similar numerical studies and grid refinement prove to be needed.

Acknowledgment

The authors acknowledge the support of the Advanced Research and Technology Program of Texas Engineering Experiment Station at Texas A&M University in developing this work.

References

[1]Von Pragenau, G., "Damping Seals for Turbomachinery," NASA TP 1987, March 1982.

[2]Al-Qutub, A., Elrod, D., and Coleman, H., "A New Friction Factor Model and Entrance Loss Coefficient for Honeycomb Annular Gas Seals," *Journal of Tribology*, Vol. 122, No. 3, 2000, pp. 622–627.

[3]Ha, T. W., and Childs, D. W., "Friction-Factor Data for Flat-Plate Tests of Smooth and Honeycomb Surfaces," *Journal of Tribology*, Vol. 114, No. 4, 1992, pp. 722–730.

[4]DeOtte, R., Morrison, G. L., Nava, D. L., and Hess, J. C., "A Study of Friction Factors in Channel Flow Between Plates with Highly Roughened Surfaces," American Society of Mechanical Engineers, FED-Vol. 195, June 1994.

[5]Childs, D. W., and Fayolle, P., "Test Results for Liquid 'Damper' Seals Using a Round-Hole Roughness Pattern for the Stators," *Journal of Tribology*, Vol. 121, No. 1, 1999, pp. 42–49.

[6]Chochua, G., Shyy, W., and Moore, J., "Computational Modeling for Honeycomb–Stator Gas Annular Seal," *International Journal of Heat and Mass Transfer*, Vol. 45, No. 9, 2002, pp. 1849–1963.

[7]Nava, D. L., "Observations of Friction Factors for Various Roughness Patterns in Channel Flow," M.S. Thesis, Turbomachinery Lab., Texas A&M Univ., Rept. TL-Seal-13-95, College Station, TX, May 1993.

[8]Hess, J. C., "Dynamic Pressure Response of Water Flow Between Closely Spaced Roughened Flat Plates," M.S. Thesis, Dept. of Mechanical Engineering, Texas A&M Univ., College Station, TX, May 1993.

[9]Villasmil, L. A., "Understanding the Friction Factor Behavior in Liquid Annular Seals with Deliberately Roughened Surfaces, a CFD Approach," M.S. Thesis, Dept. of Mechanical Engineering, Texas A&M Univ., College Station, TX, Aug. 2002.

[10]Pope, S. B., *Turbulent Flows*, Cambridge Univ. Press, Cambridge, England, U.K., 2000, Chap. 11.

[11]Chen, C. J., and Jaw, S. Y., *Fundamentals of Turbulence Modeling*, Taylor and Francis, Washington, DC, 1998, Chap. 4.

[12]Patel, V. C., Rodi, W., and Scheuerer, G., "Turbulence Models for Near-Wall and Low Reynolds Number Flows: A Review," *AIAA Journal*, Vol. 23, No. 9, 1984, pp. 1308–1319.

[13]Patel, V. C., and Chen, H. C., "Turbulent Wake on a Flat Plate," *AIAA Journal*, Vol. 25, No. 8, 1987, pp. 1078–1085.
[14]Chen, H. C., and Patel, V. C., "Near-Wall Turbulence Models for Complex Flows Including Separation," *AIAA Journal*, Vol. 26, No. 6, 1988, pp. 641–648.
[15]Wolfshtein, M., "The Velocity and Temperature Distribution in One-Dimensional Flow with Turbulence Augmentation and Pressure Gradient," *International Journal of Heat and Mass Transfer*, Vol. 12, March 1969, pp. 301–318.
[16]Patankar, S. V., Liu, C. H., and Sparrow, E. M., "Fully Developed Flow and Heat Transfer in Ducts Having Streamwise-Periodic Variations of Cross-Sectional Area," *Journal of Heat Transfer*, Vol. 99, No. 2, 1977, pp. 180–186.
[17]Villasmil, L. A., Childs, D. W., and Chen, H. C., "Understanding Friction Factor Behavior in Liquid Annular Seals with Deliberately Roughened Surfaces," *Journal of Tribology*, Vol. 127, No. 1, 2005, pp. 213–222.

S. Aggarwal
Associate Editor

Color reproductions courtesy of Texas A&M University.